

GALAXY–GALAXY LENSING IN THE HUBBLE DEEP FIELD:
THE HALO TULLY-FISHER RELATION AT INTERMEDIATE REDSHIFT

MICHAEL J. HUDSON¹ & STEPHEN D. J. GWYN

Department of Physics & Astronomy, University of Victoria,
P.O. Box 3055, Victoria, B.C. V8W 3P6, Canada
E-mail: hudson, gwyn@uvaastro.phys.uvic.ca

AND

HÅKON DAHLE & NICK KAISER

Institute for Astronomy, 2680 Woodlawn Drive, Honolulu, HI 96822, USA
E-mail: dahle, kaiser@ifa.hawaii.edu

ApJ, in press

ABSTRACT

A tangential distortion of background source galaxies around foreground lens galaxies in the Hubble Deep Field is detected at the 99.3% confidence level. An important element of our analysis is the use of photometric redshifts to determine distances of lens and source galaxies and rest-frame B -band luminosities of the lens galaxies. The lens galaxy halos obey a Tully–Fisher relation between halo circular velocity and luminosity; the typical lens galaxy, at a redshift $z = 0.6$, has a circular velocity of $210 \pm 40 \text{ km s}^{-1}$ at $M_B = -18.5$, if $q_0 = 0.5$.

Control tests, in which lens and source positions and source ellipticities are randomized, confirm the significance level of the detection quoted above. Furthermore, a marginal signal is also detected from an independent, fainter sample of source galaxies without photometric redshifts. Potential systematic effects, such as contamination by aligned satellite galaxies, the distortion of source shapes by the light of the foreground galaxies, PSF anisotropies, and contributions from mass distributed on the scale of galaxy groups are shown to be negligible.

A comparison of our result with the local Tully–Fisher relation indicates that intermediate-redshift galaxies are fainter than local spirals by $1.0 \pm 0.6 B$ mag. at a fixed circular velocity. This is consistent with some spectroscopic studies of the rotation curves of intermediate-redshift galaxies. This result suggests that the strong increase in the global luminosity density with redshift is dominated by evolution in the galaxy number density.

Subject headings: galaxies: halos — galaxies: evolution — dark matter — gravitational lensing

1. INTRODUCTION

The existence of dark matter halos around individual galaxies is now well established, but a detailed understanding of the distribution of the dark matter remains elusive. Traditional probes of the galaxy dark matter halos have been dynamical: from disk rotation curves on scales of tens of kpc, to the dynamics of globular clusters, planetary nebulae, satellites and companion galaxies on larger scales. An alternative probe of dark matter halos is the gravitational lens distortion of the shapes of background “source” galaxies. A great advantage of the lensing approach is that no assumptions about the dynamical state of the system are necessary. Clusters of galaxies have traditionally been the primary target of weak lensing studies. Galaxies are much less massive than rich clusters, and so the lensing signal is correspondingly weaker. However, the large number of lens–source pairs compensates, allowing a statistical detection of the signal. After a null detection (Tyson et al. 1984), the subject of galaxy-galaxy lensing remained dormant until the recent work of Brainerd, Blandford & Smail (1996, hereafter BBS). BBS analyzed 90 square arcmin of deep two-color ground-based images and detected galaxy–galaxy lensing from halos with typical circular velocities of 220 km s^{-1} . They studied lens–source pairs with sep-

arations of 5 to 34 arcseconds, corresponding roughly to 20 to $125 h^{-1} \text{ kpc}$ at the typical lens redshift. Recently, Dell’Antonio & Tyson (1996, hereafter DT) analyzed the Hubble Deep Field (Williams et al. 1996, hereafter HDF) and detected galaxy–galaxy lensing within 5 arcseconds of the lens galaxy, corresponding to approximately $16 h^{-1} \text{ kpc}$ at their assumed mean lens redshift.

In this paper, we investigate galaxy–galaxy lensing in the HDF. Our analysis differs significantly from that of DT, as will be shown below. A key feature of our analysis is the use of photometric redshifts derived from the four HDF colors. In §2, we describe the lens and source catalogs and the photometric redshifts. In §3, we present our maximum-likelihood method, and test it with Monte Carlo simulations in §4. Our main results are presented in §5. The characteristics of the lens sample are investigated in §6, and some potential systematics are examined in §7. Finally, in §8, we compare our results to other galaxy–galaxy lensing studies and to Tully–Fisher (hereafter TF) results from disk rotation curves at low and intermediate redshifts. We assume a cosmology with $q_0 = 0.5$ and $H_0 = 100 h \text{ km s}^{-1} \text{ Mpc}^{-1}$.

¹CITA National Fellow

2. DATA

Our galaxy catalogs are based on the wide field chips (WF2-4) of the Hubble Deep Field version 2 ‘drizzled’ images (Williams et al. 1996). As a shorthand for the F300W, F450W, F606W and F814W passbands we use U_{ST} , B_{ST} , R_{ST} and I_{ST} respectively. These magnitudes have the ST system zero-point.

2.1. Object Detection and Shape Parameters

Object catalogs were extracted using two different software packages: SExtractor version 1.0a (Bertin & Arnouts 1996) and the imcat software² of Kaiser, Squires & Broadhurst (1995, hereafter KSB). SExtractor is optimized for photometry so it was used to generate the catalog of lens galaxies. The catalog of sources was generated with imcat, which is optimized for extracting shapes of faint galaxies and other parameters relevant to lensing.

In order to avoid the edges of the chips, where image quality is poor, for both SExtractor and imcat catalogs we use only objects within the following regions: (x,y) = (182,120) to (2006,1944) of WF2; (142,192) to (1942,1992) of WF3; and (208,208) to (1976,1976) of WF4.

The lens galaxies were detected on the unsmoothed I_{ST} drizzled images. The isophotal threshold was set to twice the r.m.s. sky (corresponding to $26.65 I_{ST}$ mag/square arcsecond), and a minimum of 25 pixels were required for inclusion in the catalog. We then use the object masks generated by SExtractor to measure the fluxes within the same isophotal area in all four of the HDF passbands.

The source catalog was obtained using the imcat software on the deeper R_{ST} images, using the object detection algorithm described by KSB. This basically consists of smoothing the image with a set of ‘Mexican hat’ type filters with a range of widths, detecting peaks in the smoothed images and assigning a detection significance ν to each peak. The smoothing filter width, r_g , which gave maximum ν was found for each individual object. For our source catalog, we excluded objects with $\nu < 10\sigma$, but the true significance threshold was somewhat lower than that, since the pixel-to-pixel noise is correlated in the drizzled HDF images. We also excluded objects with half-light radius below 1.3 pixels.

For each object, we measure weighted quadrupole moments of the intensity distribution $f(\vec{\theta})$,

$$I_{ij} = \int d^2\theta W(\theta)\theta_i\theta_j f(\vec{\theta}), \quad (1)$$

where $W(\theta)$ was taken to be

$$W(\theta) = \exp(-\theta^2/2r_g^2). \quad (2)$$

From the quadrupole moments, we obtain the ellipticity polar³, $e_\alpha = \{(I_{11} - I_{22}), 2I_{12}\}/(I_{11} + I_{22})$.

The susceptibility of change of e_α of a source due to a shear γ is

$$e'_\alpha - e_\alpha \equiv P_{\alpha\beta}^\gamma \gamma_\beta, \quad (3)$$

where the prime denotes the ellipticity in the presence of a shear. In the weak lensing regime ($\gamma \ll 1$), an idealized

circular source with unweighted ($W = 1$) second moments would have $P_{\alpha\beta}^\gamma = 2\delta_{\alpha\beta}$. In practice, however, the radial weighting and the seeing both complicate this expression. Fortunately, the correct expression for P^γ is readily obtained from the observables. Luppino & Kaiser (1997) give the ‘pre-seeing shear polarizability’ as

$$P_{\alpha\beta}^\gamma = P_{\alpha\beta}^{\text{sh}} - P_{\alpha\beta}^{\text{sm}} P_{\alpha\beta}^{\text{sh}}(*)/P_{\alpha\beta}^{\text{sm}}(*), \quad (4)$$

where $P_{\alpha\beta}^{\text{sh}}$ and $P_{\alpha\beta}^{\text{sm}}$ are the post-seeing shear polarizability and smear polarizability matrices, as defined by KSB, but correcting for a minor error in their eqs. A12 and B12 (Hoekstra et al. 1997). The asterisks denote average values for stellar objects in the field. Note that this relation is only strictly valid for a Gaussian PSF, but the drizzled HDF PSFs are fairly close to Gaussian, so we chose to adopt this relation.

In practice, however, we ended up using ‘scalar’ P^γ values,

$$P^\gamma = \frac{1}{2} \left(P_{\alpha\alpha}^{\text{sh}} - P_{\alpha\alpha}^{\text{sm}} \frac{P_{\alpha\alpha}^{\text{sh}}(*)}{P_{\alpha\alpha}^{\text{sm}}(*)} \right), \quad (5)$$

where repeated subscripts denote the trace of the matrix, as these were found to be slightly less noisy than using the full $P_{\alpha\beta}^\gamma$ matrices for each individual source. We excluded sources with P^γ below 0, since these had ill-defined shape parameters. This left us with a catalog of 1622 objects.

In order to model the ellipticity distribution, we have experimented with two functional forms. The first model is just a two-dimensional Gaussian, in which the probability density distribution of each component of the ellipticity polar is given by

$$P(e)de \propto \exp\left(-\frac{e^2}{2\sigma_e^2}\right) de. \quad (6)$$

with $e \leq 1$. For the source catalog, the dispersion in ellipticity is $\sigma_e = 0.185$, independent of magnitude. The histogram of ellipticities (with both e_1 and e_2 components stacked together) is shown in Fig. 1. The Gaussian model is shown by the dotted line. This model is a good fit to the tails of the distribution, but it underestimates the number of galaxies with small ellipticity.

²Documentation for the imcat software can be found at <http://www-nk.ifa.hawaii.edu/~kaiser/imcatdoc/mainindex.html>

³Polars, unlike vectors, rotate by 2ϕ under a ϕ rotation of the coordinate axes.

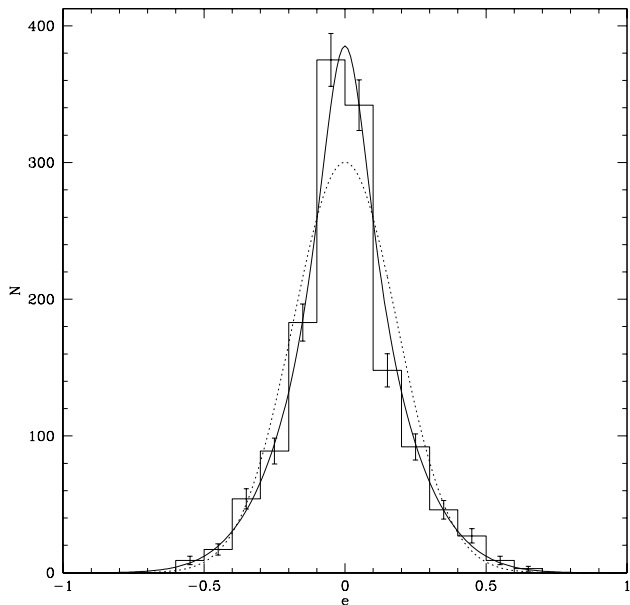


FIG. 1.— Histograms of ellipticity of source galaxies. Both e_1 and e_2 components are stacked together. The dotted curve shows the Gaussian of best fit, whereas the solid curve shows the modified Gaussian (equation [7]) of best fit.

After some trial and error, we have found a good fit using modified Gaussian model with the functional form

$$P(e)de \propto \exp\left(-\frac{e^2}{2\sigma_e'^2}\right) \times \left(1 + \frac{1}{\pi a_e} \frac{1}{(1 + (e/a_e)^2)}\right) de \quad (7)$$

with $\sigma_e' = 0.23$, and $a_e = 0.13$. This fit is shown by the solid line in Fig. 1. We adopt the Gaussian fit of equation (6) as the default in this paper, but we also consider results from the modified Gaussian.

Note that we have measured these ellipticities from the observed galaxy ellipticities, *after* they have been lensed. In principle, the correct procedure would be to use the ellipticities before lensing. In practice, however, in our model the typical shear $\gamma \ll \sigma_e$, so subtracting this shear off in quadrature makes no difference to the values derived above.

2.2. Photometric Redshifts

For every object in the lens and source catalogs, we obtain photometric redshifts as described in Gwyn & Hartwick (1996). These photometric redshifts are based on 0.2 arcsecond radius aperture photometry. The method essentially consists of converting these magnitudes to a low-resolution spectral energy distribution (SED). A set of template spectra of all Hubble types and redshifts ranging from $z = 0$ to $z = 5$ is compiled. The redshifted template spectra are reduced to the passband averaged fluxes at the central wavelengths of the observed passbands. The SED derived from the observed magnitudes of each object is

compared to each template spectrum in turn. The best matching spectrum, and hence the redshift, is then determined by minimizing χ^2 . Some improvements have been made to the method of Gwyn & Hartwick (1996): the intergalactic Lyman blanketing corrections of Madau (1995) are now incorporated; and for low redshifts ($z < 1.5$) the empirical SEDs of Coleman, Wu & Weedman (1980), as extended by Ferguson & McGaugh (1995), are used in preference over the evolving SEDs of Bruzual & Charlot (1993). Both of these corrections are found to improve the accuracy of the photometric redshifts when compared to spectroscopic redshifts.

We limit both lens and source catalogs to galaxies with isophotal I_{ST} magnitudes less than 28. If a galaxy has a spectroscopic redshift, we use this in preference to the photometric redshift. From a comparison of spectroscopic and photometric redshifts, it is found that at low redshift ($z < 1.5$) the 1σ uncertainty in z is 0.15, at high redshift ($z > 1.5$) the uncertainty is 0.35. In a recent independent test, Hogg et al. (1998) obtained spectroscopic redshifts of HDF galaxies with $z < 1.5$ and solicited photometric redshift predictions prior to publication of the spectroscopic data. The Victoria photometric redshifts were found to be accurate to $|\Delta z| < 0.3$ (0.1), 19 (15) times out of 19, when compared to high-quality spectroscopic redshifts. This is in good agreement with the errors quoted above.

For the lens catalog, we then use the redshifts to obtain absolute isophotal magnitudes in the rest-frame B -band (on the Johnson magnitude system). We wish to avoid the uncertainties of k -corrections, so for each lens galaxy we determine its rest-frame B -band magnitude by interpolation from its measured HDF magnitudes. This limits the lens catalog to the redshift range $0 \leq z \leq 0.85$. The lens catalog contains 208 galaxies. The source catalog consists of 697 galaxies with photometric redshifts, and includes the lens catalog as a subset. The top panel of Fig. 2 shows the redshift distribution of the source catalog.

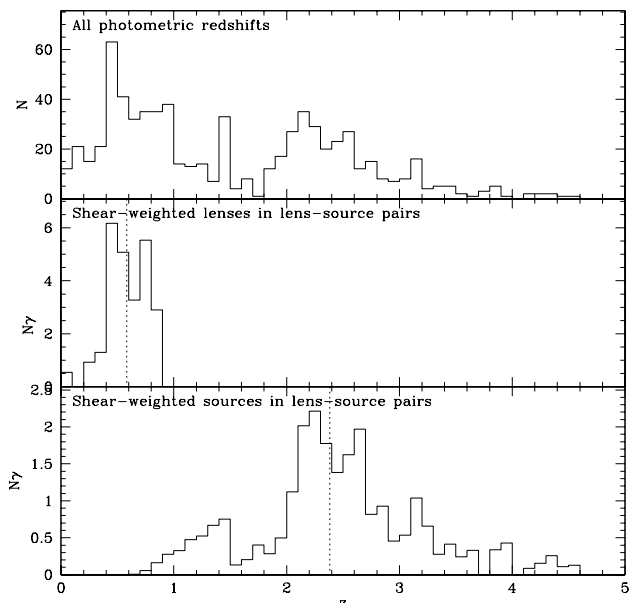


FIG. 2.— Redshift histograms. The top panel shows redshift histogram of the sample. The middle and bottom panels show the shear-weighted histogram of lens and sources respectively in all lens-source pairs (see §6 for a description of shear-weighting). The means of the weighted distributions are shown by the dotted vertical lines.

3. METHOD

In order to determine the masses of the halos, we perform a maximum likelihood analysis similar to that of Schneider & Rix (1997). The outline of this method is as follows: for a given model of the lens galaxy mass density profiles, calculate the shear at every source galaxy due to lensing by all galaxies in its foreground, thus obtain the true unlensed ellipticity. Then calculate the likelihood of this ellipticity given the ellipticity distribution determined above. A sum over all source galaxies yields a log likelihood which can be minimized with respect to the parameters of the mass model.

Our model for the galaxy dark matter halos follows BBS. Halos are assumed to be spherical singular truncated isothermal spheres with truncation radius, s , with density

$$\rho(r) = \frac{V^2 s^2}{4\pi G r^2 (r^2 + s^2)}, \quad (8)$$

where V is the circular velocity in the limit $r \ll s$ and G is Newton's constant.

It is convenient to introduce the Einstein radius for a pure isothermal sphere,

$$\begin{aligned} \theta_E &= 2\pi \left(\frac{V}{c}\right)^2 \frac{D_{ls}}{D_s} \\ &= 0.577 \left(\frac{V}{200 \text{ km s}^{-1}}\right)^2 \left(\frac{D_{ls}}{D_s}\right) \text{arcseconds} \end{aligned} \quad (9)$$

where D_s and D_{ls} are the angular diameter distances to the source and between lens and source. At typical lens and source redshifts ($z_l = 0.6$ and $z_s = 2.4$), $D_{ls}/D_s = 0.54$. For a pure isothermal sphere, the tangential shear at a separation θ is

$$\gamma_t = \frac{\theta_E}{2\theta}. \quad (11)$$

For the truncated isothermal sphere, the tangential shear, γ_t is given by (BBS):

$$\gamma_t = \gamma_0(V, s, z_l, z_s) G(\theta/\theta_s), \quad (12)$$

where $\gamma_0 = \theta_E/(2\theta_s)$, $\theta_s = s/D_l$ is the angle subtended by s , D_l is the angular diameter distances to the lens, and

$$G(X) = \frac{(2+X)(1+X^2)^{1/2} - (2+X^2)}{X^2(1+X^2)^{1/2}}. \quad (13)$$

For $X \ll 1$, $G(X) \sim 1/X$, whereas for $X \gg 1$, $G(X) \sim 2/X^2$.

The shear polar, γ_α , is then $\{-\gamma_t \cos(2\phi), -\gamma_t \sin(2\phi)\}$ where ϕ is the position angle of the line joining the lens and source galaxies. The negative sign accounts for the fact that the shear is in the tangential direction.

For each lens galaxy, we obtain the circular velocities, V , by assuming that the dark matter halos follow a Tully-Fisher relation of the form

$$V = V_f \left(\frac{L}{L_f(z)}\right)^\eta, \quad (14)$$

where V_f is the circular velocity of a galaxy with fiducial luminosity $L_f(z)$, and η is the slope of the relation. We allow for luminosity evolution of the lenses by assuming that the fiducial luminosity scales with redshift as

$$L_f(z) = L_f(z = 0.6) \left(\frac{1+z}{1.6}\right)^\zeta, \quad (15)$$

where $L_f(z = 0.6)$ is the fiducial luminosity of the Tully-Fisher relation at $z = 0.6$, which is close to the effective mean redshift of the lenses. We adopt $M_f(z = 0.6) = -18.5$, close to the effective mean magnitude of the lenses (see §6 below).

Finally, following BBS, we scale the truncation radius $s = s_{200}(V/200 \text{ km s}^{-1})^2$. However, our results below will show that s_{200} is not well constrained. We have also experimented with a linear scaling relation ($s \propto V$) but find that the resulting V_f differs by less than 2 per cent.

For all lens-source pairs used in the analysis, the predicted shear $\gamma \ll 1$, and is typically ~ 0.02 . In the weak shear limit, it is valid to calculate the total predicted shear, γ_j , at a source galaxy j via a linear sum over the contributions γ_{ij} due to all foreground galaxies i :

$$\gamma_j = \sum_i \gamma_{ij}(R_{ij}, V_i, s_i, z_i, z_j) \quad (16)$$

where the sum extends over all galaxies with $z_i < z_j$. In practice, we use only those pairs with a minimum redshift separation of 0.5 and projected separations at the

lens $R > 10 \text{ h}^{-1} \text{ kpc}^4$. Finally, we limit the sample to pairs with an angular separations less than 30 arcseconds, so that most pairs fall within the same WF chip. The motivation for the latter cut is discussed further in §7.2. There are 10156 such lens-source pairs.

The ellipticity of a given source galaxy in the absence of lensing is just $e_j = e'_j - \gamma_j P_j^\gamma$. The likelihood is then simply the probability of the corrected (unlensed) ellipticity given the measured distribution of ellipticities of galaxies in the HDF.

For the Gaussian ellipticity distribution (equation 6), a simple sum over all source galaxies yields a log likelihood

$$\log \mathcal{L} = \sum_j \left(-\frac{|e'_j - \gamma_j P_j^\gamma|^2}{2\sigma_e^2} \right) \quad (17)$$

which is maximized by varying the free parameters V_f , s_{200} , η and ζ . The quantity $2(\log \mathcal{L}_{\max} - \log \mathcal{L})$ has a χ^2 distribution with the number of degrees of freedom equal to the number of free model parameters. We can evaluate the significance of the galaxy-galaxy lensing signal by comparing the likelihood with that obtained by setting $V = 0$:

$$\chi^2 = 2(\log \mathcal{L}_{\max} - \log \mathcal{L}_{V=0}). \quad (18)$$

Note that the shear for any one lens-source pair is small compared to the intrinsic scatter in galaxy shapes. As a result, the lensing signal is an average over many pairs; no single lens-source pair dominates. In essence, our method adjusts the parameters of the TF relation, which in turn modifies the predicted tangential ellipticities, until they agree *in the mean* with the observed tangential ellipticities. In principle, one could also measure the scatter in the TF relation by subtracting in quadrature the dispersion in the ellipticity component measured along the axis oriented 45° from the line connecting lens and source from the dispersion in the tangential ellipticity component. In practice, however, the intrinsic ellipticity dispersion is much larger than the scatter in predicted shear. As a result, one cannot easily measure any source of scatter, be it intrinsic (scatter in the TF relation, aspherical halos or other random deviations from the assumed isothermal) or observational (magnitude errors, redshift errors).

The mass model presented produces an unrealistic shear field for the following reason: because the model assigns mass to galaxies within the HDF area, and no mass outside the HDF area, there is a change in the surface mass density across the HDF boundary, the smoothness of which depends on the scale size s_{200} of galaxy halos. This leads to a spurious shear near the HDF boundary.

We correct this bias by adding, for each lens-source pair, 1000 ‘mock’ lenses with the same s and z_1 . These mock lenses are placed outside the HDF area but within a radius equal to the distance from the source to the farthest edge of the HDF area. The mock lenses are assigned a V such that the mean surface mass densities of the HDF lenses and the mock lenses are equal. The circular symmetry

guarantees that there is no mean shear due to the mean density field. The large number of mock lenses guarantees that the mock lenses do not act as an additional source of noise.

Of course, in reality there will also be density fluctuations outside the HDF area. This large-scale structure will generate a slowly-varying shear across the HDF field. The addition of the mock lenses only corrects the surface mass density outside the HDF area to that within the HDF area, it does not account for possible fluctuations. The effect of such large-scale shear is examined in §7.5.

4. MONTE-CARLO SIMULATIONS

In order to test for potential biases in the maximum likelihood method, we have run a series of Monte Carlo simulations. We choose galaxies with redshifts from the observed distribution, but assign random positions within a circular area which is much larger than the HDF area. We then adopt a TF relation and assign circular velocities and truncation radii to the lenses based on their absolute magnitudes. Galaxies are assigned ellipticities drawn from equation (6). Each galaxy’s ellipticity parameters are then perturbed by *all* foreground galaxies. Thus our Monte Carlo simulations contain extra sources of shear which affect the real data, namely lenses outside the HDF area and lens-source pairs with separations less than $10h^{-1} \text{ kpc}$ or with redshift separations less than 0.5. From this supersample, only the lenses (restricted to $0 < z < 0.85$) and sources within the HDF area are output. These catalogs are then analyzed as described above for the real data. In our simulations we used $V_f = 200 \text{ km s}^{-1}$, $s_{200} = 100h^{-1} \text{ kpc}$ and $\eta = 0.25$.

The Monte Carlo simulations show that the maximum-likelihood method described above recovers unbiased values of V_f ($\lesssim 5\%$) and η . The returned values of s_{200} are also unbiased, but have a very large scatter, indicating that it is very difficult to constrain this parameter. Furthermore, the recovered values of V_f and s_{200} are slightly anti-correlated in the sense that the halo mass within a radius of $\sim 30h^{-1} \text{ kpc}$ is the most tightly constrained combination. If we do not add mock lenses outside the HDF area, we recover essentially unbiased results for V_f but s_{200} is biased low by a factor ~ 5 .

We can also use the Monte Carlo simulations to test the effect of the random errors in the photometric redshifts. We proceed as above, except that we add errors to the redshifts as follows. First, we add a random Gaussian error of 20% in z . Then we allow for non-Gaussian tails in the error distribution by assigning a redshift at random within the range 0 to 5 for 10% of the galaxies. We use the perturbed photometric redshifts to adjust absolute luminosities accordingly. We find no significant bias in the recovered value of V compared with the simulations with no redshift errors. This occurs because, for a lens galaxy of fixed apparent magnitude and a source at a fixed separation from it on the sky, as the redshift increases, L and hence V increase but there is a compensating decrease in

⁴Note that a given source galaxy is not excluded from the analysis if it passes within less than $10 \text{ h}^{-1} \text{ kpc}$ of a lens galaxy. However, the shear for that particular lens-source pair is not included in equation (16). Note that the position angle of such close pairs is uncorrelated with the position angles of the pairs which are included in the sum, so that no bias arises from excluding such pairs. The shear due to the close encounter will increase the scatter in ellipticity of such sources. This shear is negligible in comparison to the intrinsic scatter unless the encounter is within a few Einstein radii, $\sim 0.75 \text{ arcseconds}$ or $\sim 3h^{-1} \text{ kpc}$ for a typical lens. We estimate that only a few per cent of sources are significantly affected in this way.

the ratio D_{ls}/D_s . For the default case $\eta = 0.25$ and for the typical lens and source redshifts studied here, the two terms very nearly cancel.

However, we do find a small bias in the recovered TF slope: $\eta = 0.22 \pm 0.01$ compared with the input $\eta = 0.25$. This bias is much smaller than the random errors, so we neglect it in this analysis.

5. RESULTS

When we fix $s_{200} = 50h^{-1}$ kpc, $\eta = 0.35$ (as found for the local B -band TF), and $\zeta = 0$ (i.e. no evolution), we obtain our main result

$$V_f = 210 \pm 40 \text{ km s}^{-1} \quad (19)$$

For this solution, we obtain $\chi^2 = 7.2$, which is significant at the 99.3% confidence level (2.7σ). The error bars have been determined in the usual way, i.e. they correspond to $\chi^2 - \chi_{min}^2 = 1$. Note that the control tests of §7.1 confirm that the χ^2 statistic is indeed correct. We then allow each of the parameters η , s_{200} and ζ to be free in turn. The best fit values are $\eta = 0.62$, $s_{200} = 12.2h^{-1}$ kpc (with $V_f = 250 \text{ km s}^{-1}$) and $\zeta = 1.88$, but in each case the change in χ^2 is not statistically significant compared to the increase of 1 degree of freedom. Fig. 3 shows the joint likelihood contours for V_f and each of s_{200} , η and ζ , with the other two parameters held fixed at their fiducial values. The joint likelihood of η and ζ is also shown. Note that a flat ($\eta = 0$) TF relation, corresponding to constant circular velocity independent of luminosity, is not favored by the data.

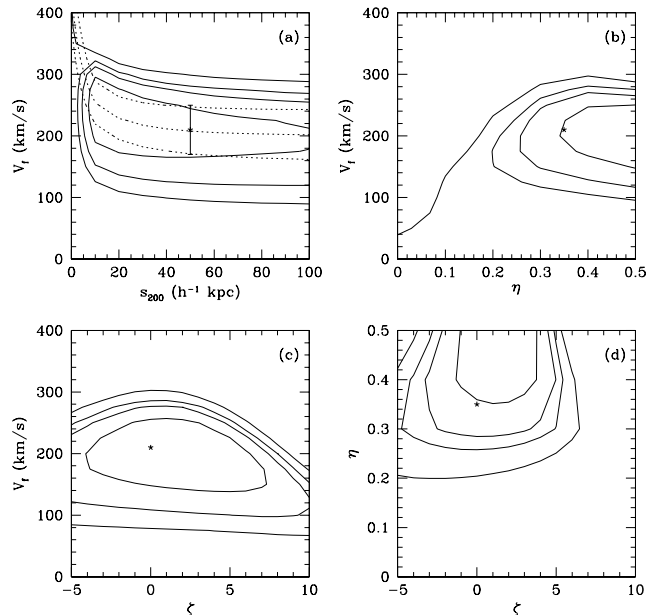


FIG. 3.— Likelihood contours for various combinations of parameters. Contours indicate the 68, 90, 95 and 99% confidence limits on two parameters jointly. (a) The V_f – s_{200} plane. The star shows the fiducial choice of s_{200} and the best fit value of V_f and 1σ errors. The three dotted lines show models of constant mass within $30 h^{-1}$ kpc, equal to $2.8 \pm 1.2 \times 10^{11} h^{-1} M_\odot$. (b) V_f and η (c) V_f and ζ (d) η and ζ with $V_f = 200 \text{ km s}^{-1}$.

In Fig. 3a, the dotted lines show the loci of truncated isothermal models with constant mass within $30 h^{-1}$ kpc, M_{30} . These lines run close to the isolikelihood lines. Our solution corresponds to $M_{30} = 2.8 \pm 1.2 \times 10^{11} h^{-1} M_\odot$. The corresponding B -band mass-to-light ratio within this radius is $75 \pm 30 h (M/L_B)_\odot$. However, since we cannot constrain the total extent of the halos, this number should be taken as a lower limit to the mass-to-light ratio of galaxies.

For the ellipticity distribution (7), we obtain similar results: $V_f = 235 \text{ km s}^{-1}$, with $2(\log \mathcal{L}_{max} - \log \mathcal{L}_{V=0}) = 11.7$. However, because equation (7) is not a Gaussian, this likelihood statistic is no longer simply related to χ^2 , and hence it is difficult to evaluate the significance of this result and its error. However, the tests described in §7.1 below indicate that the significance of this result is slightly better than for the default Gaussian distribution used above. Consequently, the error bars are likely to be similar to those quoted above.

6. CHARACTERISTICS OF THE LENS SAMPLE

In order to interpret our results, it is important to know the properties of the galaxies which dominate the lensing signal. The composition of the lens catalog itself does not accurately reflect the galaxies which dominate the lensing signal because several factors, most importantly luminosity and redshift, determine whether a galaxy is an efficient lens. In general, the lens-source pairs with the highest predicted shear, $|\gamma_{t,ij}|$, should have the greatest effect on

the likelihood. We can therefore determine the ‘effective’ mean, \tilde{x} , of any quantity x by weighting the lens-source pair $w_{ij} = |\gamma_{t,ij}|$:

$$\tilde{x} = \frac{\sum_{ij} w_{ij} x}{\sum_{ij} w_{ij}}. \quad (20)$$

We will use this shear-weighting method to determine the radial dependence of the lensing signal, and to obtain the typical redshifts, magnitudes and colors of the lens galaxies.

We can get an impression of the radial dependence of the galaxy-galaxy lensing signal by calculating the effective mean tangential ellipticity of the sources in all lens-source pairs as a function of separation in h^{-1} kpc. The ellipticities are weighted according to the predicted shear, as described above. This is plotted in Fig. 4 with the predictions corresponding to combinations of V_f and s_{200} in the maximum likelihood valley of Fig. 3a. The small difference in the shapes of these curves illustrates the difficulty of constraining s .

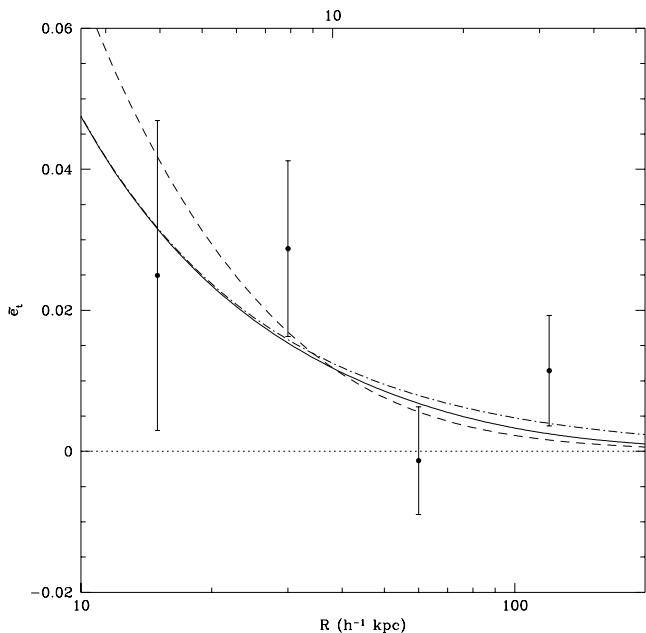


FIG. 4.— The weighted mean tangential ellipticity of sources around all lenses as a function of separation in h^{-1} kpc. The top axis gives the separation in arcseconds for $z_l = 0.6$. The weight for each pair is proportional to the predicted tangential shear; see text for details. The solid curve shows the change in ellipticity of a source at $z_s = 2.4$ due to gravitational shear of a lens at $z_l = 0.6$ for the fiducial model $V_f = 210 \text{ km s}^{-1}$, $s_{200} = 50 h^{-1} \text{ kpc}$. The dashed curve shows a model with $V_f = 250 \text{ km s}^{-1}$, $s_{200} = 12.5 h^{-1} \text{ kpc}$ and the dot-dash line shows a singular isothermal sphere with $V = 210 \text{ km s}^{-1}$ and no truncation radius.

We can also use shear-weighting to determine the characteristics of lens and source galaxies. The effective mean redshifts are $\tilde{z}_l = 0.6$ and $\tilde{z}_s = 2.4$. The weighted lens and source redshift histograms are shown in the lower two panels of Fig. 2. The effective mean lens magnitude is $\tilde{M}_B = -18.5$. The lensing signal arises equally from 2 sub-samples: 14 bright lenses with $M_B \lesssim -18.5$ (the brightest

of which has $M_B = -20.3$) and the remaining 194 faint lenses with $M_B \gtrsim -18.5$ (mean -17.5 , but with a tail extending to -15). It is worth noting that no single lens galaxy is responsible for the entire signal detected here. The lens galaxy with the most impact on the solution is the $I_{ST} = 20.87 \text{ mag}$, $z = 0.518$ galaxy at $x = 1396$, $y = 1167$ on WF3. Our result remains significant, however, if this galaxy is removed. The shear-weighted shear for a typical lens-source pair is $\tilde{\gamma}_{ij} \sim 0.02$, and hence the sample contains the equivalent of $\tilde{N}_{ls} \sim 1000$ of such pairs. In a similar fashion, we infer that the effective number of lenses is $\tilde{N}_l \sim 40$. The effective mean pre-seeing shear polarizability is $\tilde{P}\gamma = 0.74$.

We have also investigated the morphological types and colors of the lens galaxies. Morphological classifications are available only for the brightest ($I < 25$) HDF galaxies (van den Bergh et al. 1996). We have identified all galaxies classified as E or S0 by both van den Bergh and Ellis. We have compared results obtained from the $I < 25$ subsample of our lens sample (73 galaxies) with and without the 11 early-type galaxies. We find only a 3% drop in V_f when the early-type galaxies are excluded, although the significance of the result drops slightly, to the 2.5σ level.

We have also measured rest-frame $U-B$ colors of the HDF lens galaxies and compared these with the colors of early-type galaxies ($T < 0$) from RC3. Approximately 90% of early-type galaxies in RC3 have $U-B > 0.23$. If the stars in ellipticals were formed at high redshift, then we expect passive evolution to shift this limit to $U-B > 0.12$ at $z = 0.6$ (Worthey, 1994). The median rest-frame $U-B$ color of the 11 morphologically classified early-type galaxies is 0.15. In the HDF lens sample, only 11% of galaxies have $U-B > 0.12$. This fraction is similar to the fraction (13%) of galaxies classified morphologically as E or S0. If these red galaxies are excluded from the lens catalog, V_f is unchanged. Thus selection by morphology and selection by color both lead to the conclusion that our result is not affected by presence of a small fraction of early-type galaxies. In general, there is little evidence of color dependence. The red half of the sample has a higher V than the blue half by only 16 ± 32 per cent. Larger samples are required to test the color dependence in more detail.

In summary, we conclude that the lensing signal is dominated by spiral galaxies at $z \sim 0.6$, with luminosities 1 mag. below L_* . Thus our lens sample is similar to the I -band limited CFRS redshift survey (Lilly et al. 1995).

7. POSSIBLE SYSTEMATIC EFFECTS

This section describes tests performed to explore possible systematic effects which might bias our results.

7.1. Control Tests

We have performed a number of control tests in order to verify the reality of the signal. If we rotate the source position angles by 45° we expect no signal, and indeed we find none. We have also experimented with randomizing the position angles of the sources, and with randomizing the positions of the sources and lenses. For each of these tests, we generate 1000 such random realizations. We obtain a signal as significant as the observed signal in 18,

17 and 2 cases, respectively. These tests confirm that our result is significant at the 99% confidence level, in agreement with the significance level obtained directly from the χ^2 distribution.

If we adopt the modified Gaussian ellipticity distribution (equation 7), we find that the number of false positives is reduced by a factor of 2, leading to an improved significance level of 99.5%.

We have also examined the subsample of 925 sources with $I_{ST} > 28$. These galaxies are too faint to have reliable photometric redshifts. However, they can still be used, albeit with loss of precision and some systematic uncertainties. We have performed Monte Carlo simulations in which the faint galaxies are assigned redshifts drawn at random from the redshift distribution of bright sources. For any one realization, we do not necessarily obtain a significant detection, but when the χ^2 values are averaged over all realizations we find a minimum with $\chi^2 = 3.5$ at $V_f = 165_{-45}^{+35}$ km s $^{-1}$. Thus, from the faint sources alone, we detect a marginally significant signal (at the 94% confidence level) and a value of V_f which is consistent with that found from the brighter sources. However, we prefer not to place too much weight on the derived value of V_f since it depends on the uncertain redshift distribution of these very faint source galaxies⁵. The significance of the detection should be less sensitive to the shape of redshift distribution, so we take this result as independent confirmation of our detection using the brighter sources. Taking both bright and faint results together, the significance of the detection is 99.8%. It would appear that photometric redshifts increase the statistical weight of sources by a factor ~ 3 relative to no redshift information.

7.2. Effects of PSF Anisotropies

It is likely that the drizzling algorithm does not completely remove the anisotropy of the HST PSF. We have examined the mean ellipticity of source galaxies measured tangentially to the chip center, as a function of radius from the center. We find a weak, marginally significant (2σ), and approximately linear trend with radius. The mean tangential ellipticity increases from zero at the center to 0.018 ± 0.008 at the edge. (Note that we find no mean ellipticity tangential to the *field* center.) This anisotropy is in the same sense as that found by Hoekstra et al. (1997), although the amplitude is apparently somewhat smaller for than they found for undrizzled HST images. In order to test how this might affect our results, we have constructed a modified source catalog with the mean trend subtracted from the measured ellipticities. The difference in mean tangential ellipticity between the modified catalog and the original catalog is negligible except for pairs with separations $\gtrsim 30$ arcseconds (\gtrsim half the WF chip size). Consequently, we find that this modification has no effect on the value of V_f . However, for the modified ellipticity sample, the very large separation (> 30 arcseconds, roughly equivalent to $> 100h^{-1}$ kpc) pairs tend to have negative mean tangential ellipticities. If these pairs are used in the analysis, the likelihood derived from the modified source catalog marginally favors mass models with small truncation radii,

$s_{200} \sim 5 h^{-1}$ kpc with a corresponding increase in V_f (see, for example, the dashed line in Fig. 4). Such models are preferred because the predicted shear goes to zero more quickly at large radii. This preference for small truncation radii does not occur with the original ellipticities, or for either sample if pairs are limited to a maximum of 30 arcseconds separation. Ultimately, we do not know whether the trend found above is an uncorrected anisotropy or not. We prefer avoid this issue by limiting the sample used in this paper to the robust pairs with separations < 30 arcseconds.

7.3. Isophotal contamination

One possible concern is that the extended luminosity profile of bright galaxies might affect the measured shapes of the faint galaxies in their wings. We have explored this possibility by adding artificial faint galaxies in the wings of bright ($I_{ST} < 25$) HDF galaxies, using the IRAF artdata/mkobjects package. The artificial galaxies have a range of sizes, surface brightnesses and ellipticities consistent with those in our source catalog. The simulated source galaxies are placed with random position angles and at various radii from the centroids of the bright HDF galaxies. We then extract their image parameters using imcat and compare these to the input parameters.

⁵Note that if the faint sources are in fact at greater distances than the bright sources, as is likely, then by this procedure we have underestimated D_{ls}/D_s and hence have overestimated V_f . However, the correction factor is likely to be small: if, for example, the faint sources lie at a typical z of 3 (versus 2.4 for the bright sources), then V_f is overestimated by only 3 per cent.

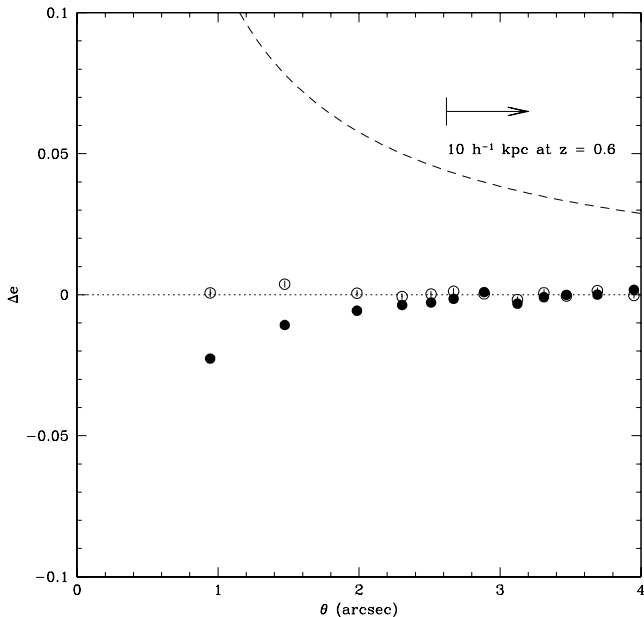


FIG. 5.— A simulation of the effect of light contamination from foreground galaxies on the shape parameters of background galaxies. The change in imcat ellipticity of simulated source galaxies is plotted as a function of separation from bright galaxies ($I_{ST} < 25$). Solid points indicate the change in ellipticity along the direction tangential to the line joining the pair. Open points show the change in the direction rotated by 45° . These are consistent with zero as expected. The dashed line shows the expected change in ellipticity due to weak lensing from a lens with $V = 200 \text{ km s}^{-1}$ at $z = 0.6$ on a background source at $z = 2.4$. Note that the contamination effect is small and goes in the opposite sense to the lensing signal: galaxies tend to be biased towards radial alignments.

Fig. 5 shows the median change in imcat ellipticity as a function of projected separation in arcseconds. The solid points show the change ellipticity along the tangential direction, and the open symbols show the change along a direction rotated by 45° . For comparison, the dashed line shows the change in tangential ellipticity due to a $V = 200 \text{ km s}^{-1}$ isothermal sphere at $z_l = 0.6$ for source at $z_s = 2.4$. From Fig. 5 it can be seen that the effect is of opposite sign to the effect of gravitational lensing: isophotal contamination distorts the faint objects in the radial direction. A very similar effect is found for ellipticities measured with SExtractor. The effect is many times weaker than the effect of gravitational lensing at all radii and is completely negligible for the minimum separation of $10h^{-1} \text{ kpc}$ (~ 2.5 arcseconds) used here. We are therefore justified in neglecting this effect.

7.4. Satellites and Spiral Arms

Another potential systematic effect is the contamination of the source catalog with satellite galaxies or spiral arm segments which have been treated as separate objects by the object finding software. It is not known whether satellites tend to be preferentially tangentially oriented with respect to the primary, but spiral arm segments certainly would be. If such objects are included in the source catalog, they could bias the results.

We can use cuts in projected separations to test for such contamination. The default minimum projected metric separation is $10h^{-1} \text{ kpc}$. However, as a check, we have experimented with minimum separations in units of the major-axis second moment. When the minimum separation is set to 5 times the major-axis second moment (equivalent to ~ 8.7 exponential disk scale-lengths), we find an equally strong lensing signal. Since this separation is well beyond the optical radius, there is little chance that spiral arms are contaminating our signal.

A great advantage of this study arises from the use of photometric redshift data, which allows us to cleanly separate foreground and background objects. Note that we impose a minimum redshift separation between lens and source of 0.5, which corresponds to ~ 3 times the photometric redshift error at the effective lens redshift of 0.5. It is worth noting that if the minimum redshift separation is decreased to 0, the significance of our result increases to 3σ and V_f increases by 5%. However, if the minimum redshift separation is increased to 1, we still find a significant signal. These tests confirm that our results are not biased by objects at the same redshift as the lens.

7.5. Effects of Large-Scale Structure

It is well known that a uniform sheet of mass produces no shear, and hence cannot bias our results. In §3, however, we noted that density fluctuations near the HDF would give rise to a slowly-varying shear across the HDF field. If the lens-source pairs sample all position angles uniformly, it is easy to show that a uniform shear field, or one with a constant gradient, will drop out. Thus we expect that the slowly-varying signal expected from large-scale structure will not affect our results.

By taking the mean of the ellipticities on all three WF chips, we find a marginally significant tendency for galaxies to be elongated in the x -direction (i.e. along the line connecting the bases of chips WF3 and WF4) with mean ellipticity 0.014 ± 0.007 . If this were due to large-scale shear, the corresponding value of γ would be 0.02 ± 0.01 . This is in good agreement with the r.m.s. mean shear expected in the non-linear regime (i.e. on scales of 1 arcmin) from sources at $z = 2$ (~ 0.03 , Jain & Seljak 1997). Alternatively, it may arise from incorrect registration during the drizzling procedure. In either case, it is interesting to know whether this may bias our results. If we subtract off the mean ellipticity, we find that V_f is unchanged. Note that for pairs with larger separations, the lens-source position angles are no longer random. The largest separations are dominated by pairs between WF2 and WF4, which have lens-source position angles $\pm 45^\circ$. Nevertheless, even if we include these large separation pairs, our V_f result is essentially unaffected.

7.6. Effect of correlated dark matter on intermediate scales

It is also possible our results might be biased by mass concentrations other than the halos of the observed HDF galaxies. It is easy to see that dark matter concentrations which are uncorrelated with the observed galaxies will not affect our results: the shear produced by such concentrations will add scatter to the source ellipticities

— something which is difficult to separate from the intrinsic scatter in ellipticity — but will add no net tangential shear. On the other hand, dark matter which is correlated with bright galaxies could potentially bias our results. We consider here two possible sources: undetected galaxies which are clustered with the observed galaxies in the lens sample, and dark matter on group scales.

From the spatial two-point correlation function for galaxies, we can calculate the mean excess number of $\sim L_*$ neighbors within a given distance of a galaxy. The distance where that mean excess is unity is approximately $300 h^{-1}$ kpc at the present epoch, and at smaller distances the probability of having a correlated neighbor is small. At high redshift, one has to allow for evolution: the number density goes up, but the correlation amplitude goes down, roughly compensating. For the $\sim 30 h^{-1}$ kpc scale which dominates our signal, the probability of finding a neighbor remains small. Furthermore, note that at $z \sim 0.6$, all galaxies with $M_B < -15$ are included in the lens sample and hence in the mass model. Thus the contamination from galaxies fainter than this limit will be smaller still.

Another candidate for correlated dark matter is the dark matter distributed in the groups and clusters in which (at least some of) these galaxies dwell. We have examined the effect of group-scale dark matter concentrations on our results. Specifically, we have calculated the mean tangential shear around a galaxy, as a function of galactocentric radius R , due to a spherically symmetric group located at a distance R_{gr} away from the galaxy. The group is assumed to have a truncated isothermal mass density profile. Clearly, if $R_{\text{gr}} = 0$ then the circular velocity of the group dominates the contribution from the galaxy. On the other hand, for large values of R_{gr} , we find that the group typically has a negative effect on the mean tangential shear over the range of galactocentric radii considered here. This is illustrated graphically in Fig. 6. The overall net effect depends on the distribution of galaxies with respect to the group center, i.e. on the distribution of R_{gr} . If galaxies are unclustered with respect to the group center, then there is no net effect, for the reasons given above. If on the other hand, galaxies are distributed like the group dark matter, that is as r^{-2} , or R^{-1} in projection, then the group contributes a small net positive contribution to tangential shear, the amplitude of which is independent of R and which depends on the circular velocity and cut-off radius of the group. We find that, for our maximum likelihood method and default parameters, the bias to the galaxy circular velocity is $\sim 0.02 (V_{\text{gr}}/V)^2 [s_{\text{gr}}/(300 h^{-1} \text{ kpc})]^{-1}$, with a weak dependence on the assumed s .

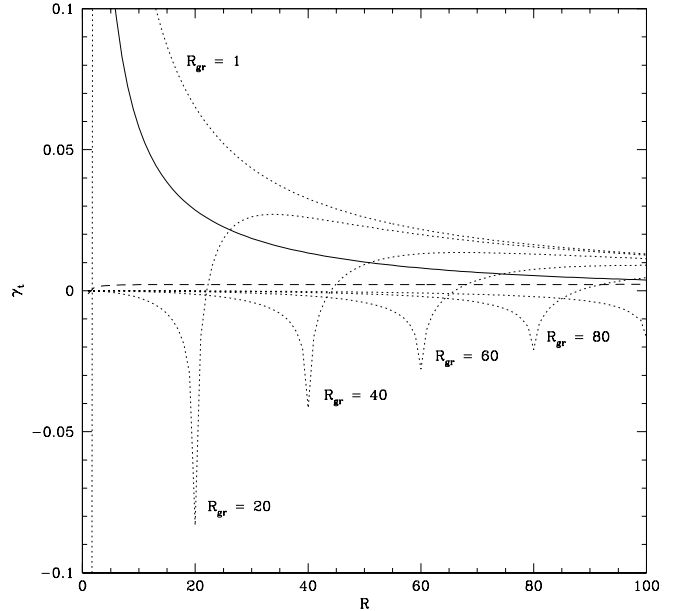


FIG. 6.— The tangential ellipticity with respect to a galaxy as a function of galactocentric radius R due to a $V = 200 \text{ km s}^{-1}$ galaxy (solid line) and the contributions from a group with $V_{\text{gr}} = 300 \text{ km s}^{-1}$ and truncation radius $s_{\text{gr}} = 300 h^{-1} \text{ kpc}$, where the galaxy lies at separations $R_{\text{gr}} = 1, 20, 40, 60, 80, 100 h^{-1} \text{ kpc}$ from the center of the group (dotted lines). The dashed line shows the mean contribution from the group averaged over all galaxies in the group, if the galaxies are distributed like the mass in the group.

To apply this formula, we need the typical circular velocity dispersion of groups as well as their typical sizes. While the *pair-weighted* r.m.s. velocity dispersion of galaxies is $540 \pm 180 \text{ km s}^{-1}$ (Marzke et al. 1995), this value is not representative of the field because it is biased by the large number of pairs in rich clusters. A single-galaxy weighted estimate of the line-of-sight velocity dispersion of field galaxies with respect to their local $2 h^{-1} \text{ Mpc}$ neighborhood is $\sim 100 \text{ km s}^{-1}$ (Davis, Miller & White 1997). If all field galaxies are assumed to lie in groups then the corresponding circular velocity of the group would be $\sim 150 \text{ km s}^{-1}$. A more realistic assumption might be to assign 50% of galaxies to groups with typical circular velocities of $\sim 250 \text{ km s}^{-1}$. In either case, the mean bias is identical: it is negligibly small.

8. DISCUSSION

8.1. Comparison with previous galaxy–galaxy lensing results

Our results are in good agreement with the original detection of BBS, who found $V_f = 220 \pm 80 \text{ km s}^{-1}$ for a fiducial $M_V = -20.3$ galaxy⁶ (with TF slope $\eta = 0.25$). If we adopt a mean rest-frame $B - V$ color of 0.6 for galaxies at $z \sim 0.4$, then the BBS fiducial magnitude corresponds to $M_B = -19.7$. Scaling their V_f to our fiducial magnitude ($M_B = -18.5$) with $\eta = 0.25$ then yields $165 \pm 60 \text{ km s}^{-1}$. This is consistent with our result. Note that BBS make

⁶The fiducial magnitude $M_r = -18.5$ quoted in BBS is incorrect (T. Brainerd, private communication).

no correction for the circularization of their sources due to seeing. As a result they will tend to underestimate the shear and hence the circular velocities of the lens galaxies.

At face value, our results also agree well that of DT who found $\langle V \rangle = 260 \pm 45 \text{ km s}^{-1}$. However, our analysis differs significantly from theirs in a number of ways. We use photometric redshifts and scale V according to the TF relation, whereas DT adopted a constant V for all bright ($22 < I < 25$) galaxies, and assumed a redshift distribution for lenses and sources. If, following DT, we also assume a flat ($\eta = 0$) TF relation, we do not detect a significant signal. This may be a result of the different range of projected separations probed: DT use separations less than 5 arcseconds, which corresponds to $16 h^{-1} \text{ kpc}$ at their mean lens redshift of 0.4, whereas we specifically limit our sample to separations larger than $10 h^{-1} \text{ kpc}$.

8.2. Comparison with the Tully-Fisher relation

In §5, we found that our sample was not capable of measuring the B -band evolution of the TF relation based on the HDF data alone. In §6, we showed that our signal was dominated by spiral galaxies with luminosities 1 mag. below L_* . It is therefore interesting to compare our result to the Tully-Fisher relation derived from HI linewidths nearby and optical rotation curves at intermediate redshifts. However, in order for this comparison to be valid, we must first address two technical issues (corrections to total magnitudes and inclination corrections) and the more general issue of the flatness of the rotation curves at large radii.

The magnitudes in our lens catalog are isophotal, whereas total magnitudes are used in Tully-Fisher studies. At the typical lens galaxy redshift of 0.6, the limiting I_{ST} isophote is close to a rest-frame isophote of $25 B \text{ mag/square arcsecond}$. At low redshift, the correction from this isophotal magnitude to total B magnitude is only 0.11 mag. for spiral galaxies (de Vaucouleurs et al. 1991, hereafter RC3). Note that the correction from isophotal magnitude to total magnitude depends only on the central surface brightness of the galaxy and the surface brightness of the isophotal limit. For an Sbc galaxy with a bulge-to-total luminosity fraction of 0.25 and a central disk surface brightness of $21.65 B \text{ mag/square arcsecond}$, the correction is $\sim 0.15 \text{ mag}$, in reasonable agreement with the RC3 value. However, if intermediate redshift galaxies have higher central surface brightnesses by 0.5–1.0 mag., as suggested by some studies discussed below, then this correction falls to 0.10–0.07 mag. We adopt 0.1 mag. for the isophotal-to-total magnitude correction.

Our lens catalog contains galaxies of all inclinations. Rather than correct each HDF galaxy individually, we correct the fiducial magnitude using the prescription of Tully & Fouqué (1985) by averaging over all inclinations. Thus, with both corrections the fiducial face-on total magnitude is $M_B = -18.9$.

Finally, note that the lensing method probes the mass within $\sim 30 h^{-1} \text{ kpc}$, whereas studies of optical rotation curves or HI linewidths probe out to the edge of the optical or HI disks ($\sim 10 - 20 h^{-1} \text{ kpc}$). If rotation curves are not flat then an offset might be expected between the two measures. The resolved HI rotation curves of Broeils (1992) extend out to $30 h^{-1} \text{ kpc}$ for galaxies with $V > 150 \text{ km s}^{-1}$

and are flat or gently declining beyond the optical radius (see Fig. 16 of Courteau 1997). If the $H\alpha$ rotation curves of Courteau (1997) are extrapolated to $30 h^{-1} \text{ kpc}$, then for galaxies with $V \sim 200 \text{ km s}^{-1}$, V_{max} is on average $\sim 5\%$ lower than $V(r = 30 h^{-1} \text{ kpc})$. On average, we therefore expect the lensing circular velocities to be a reasonable measure to compare with HI linewidths or optical rotation curves.

For the local TF relation we use the Ursa Major B -band data from Pierce & Tully (1988). We assume a Hubble velocity of 1324 km s^{-1} for the Ursa Major cluster. For comparison, we also show the scaling relation followed by elliptical galaxies. We have used the B -band Quality ‘1’ data of Faber et al. (1989), and multiplied the central velocity dispersions, σ_c by $\sqrt{2}$ to obtain effective circular velocities. The results are plotted in Fig. 7. The HDF TF relation is shown by the hatched area.

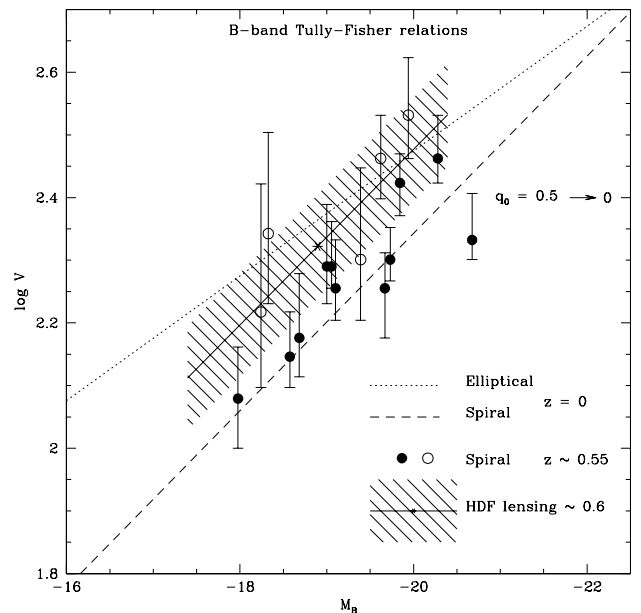


FIG. 7.— The B -band Tully-Fisher relations for nearby spirals (dashed line) and ellipticals with $V = \sqrt{2}\sigma_c$ (dotted line). The $\langle z \rangle = 0.54$ data of Vogt et al. (1996, 1997) are shown by the large circles with error bars (filled symbols for high quality data). The mean TF relation for the HDF lens galaxies at $z \sim 0.6$ is indicated by the hatched region. The horizontal extent shows the magnitude range covered by the data, and the vertical extent gives the 1σ error in $\log V$. The small arrow shows the effect on our HDF lensing solution if q_0 is changed from 0.5 to 0.

By comparing the rotation curve and lensing TF relations, we find that the HDF galaxies are fainter at a fixed V than the local TF galaxies. We thus infer $\Delta M_B = +1.0 \pm 0.6$ from $z = 0$ to $z \sim 0.6$. Equivalently, at a fixed luminosity galaxies rotate 38% faster at intermediate redshift. A brightening of more than -0.2 mag . is excluded at the 95% confidence level by our data.

If we adopt $q_0 = 0$, V_f drops to $190 \pm 35 \text{ km s}^{-1}$. Equivalently, galaxies brighten by 0.3 mag. at a fixed circular velocity compared to the $q_0 = 0.5$ case, but remain fainter than $z = 0$ spirals by $0.7 \pm 0.55 \text{ mag}$.

For comparison, we also show in Fig. 7 the intermediate redshift results of Vogt et al. (1996, 1997), converted to $q_0 = 0.5$, $H_0 = 100$ (large circles). These galaxies have $\langle z \rangle = 0.54$, close to our lens sample. Note that with this choice of cosmology, the evolution of the Vogt et al. sample with respect to the local TF relation is a dimming $\Delta M_B = +0.21 \pm 0.16$ (high quality data only) or $+0.33 \pm 0.20$ (weighted fit to all data)⁷. Our results are therefore consistent with the Vogt et al. data. Both results favor little or no luminosity evolution in the B -band for galaxies ~ 1 mag. below L_* .

This conclusion differs from those of Rix et al. (1997) and Simard & Pritchet (1998). Both of these groups found that the galaxies in their samples (at $z \sim 0.3$) were brighter than their local counterparts by ~ -1.5 mag. However, both of these samples are dominated by galaxies with large O II equivalent widths: 15 of 19 in Rix et al. and 11 of 12 of galaxies in Simard & Pritchet have equivalent widths larger than 20 \AA , indicating high rates of star formation. Clearly more local TF data, spanning a range of morphologies and star formation rates, are needed in order to understand the differences in the TF evolution of the different samples.

The total luminosity *density* is evolving strongly, $\zeta = 2.7 \pm 0.5$ in the B -band (Lilly et al. 1996). The luminosity density evolution is dominated by galaxies near L_* . Because these same galaxies dominate our lens sample, we can compare the global luminosity evolution with our result for the evolution of the Tully-Fisher relation. We can rule out (at the 3.6σ level) the possibility that the evolution found by Lilly et al. is solely due to the luminosity evolution of individual galaxies. This suggests that the evolution in the global luminosity density is not dominated by luminosity evolution of individual galaxies but rather by the evolution in their number density.

8.3. Evolution in size or luminosity?

It is interesting to compare our results with the evolution of surface brightness, which is a complementary probe of galaxy evolution.

Schade et al. (1996a) found that cluster and field ellipticals at $z \sim 0.6$ had surface brightnesses which were -0.8 mag. brighter than $z = 0$ ellipticals in the rest frame B -band. Note that if this is attributed to passive luminosity evolution then in Fig. 7, the $z = 0.6$ Faber-Jackson relation would lie on top of the $z = 0$ Tully-Fisher relation. Thus passive evolution might explain the small difference in V_f that we find between our the spiral and elliptical subsamples.

For spiral galaxies, the situation is more complicated. Schade et al. (1996b,c) find that spirals at $z \sim 0.6$ have surface brightness which are ~ -1.3 mag. brighter than at $z = 0$. Forbes et al. (1996) find -0.6 mag. for their sample at $z \sim 0.5$, while Vogt et al. find a similar increase in *surface brightness* for their TF sample. If this surface brightness evolution is attributed to luminosity evolution, then the luminosity evolution derived from lensing disagrees with the results of Schade et al. by ~ 2.2 mag, and disagrees by ~ 1.6 mag. with those of Forbes et al. and Vogt et al.

An alternative interpretation of this surface brightness evolution is that the population of disk galaxies is undergoing evolution in their characteristic sizes. Such a trend is predicted in hierarchical models if the halos of disk galaxies were assembled recently (say between $z \sim 1$ and $z \sim 0$). The density at which halos virialize is a multiple of the critical density at the time at which they collapsed. Thus, at a fixed mass, halos which collapse at a higher redshift will have higher densities than their lower redshift counterparts. If the dark matter halo determines the amplitude of the rotation curve, then the high redshift disks will have higher circular velocities at a given mass. Using the prescriptions of Mo, Mao & White (1997, see also Mao, Mo & White 1997), and assuming that the halo is assembled at the redshift at which it is observed and that the mass-to-light ratio of the disk is constant, then in an $\Omega = 1$ universe, disks of a fixed circular velocity which form at $z \sim 0.6$ will have scale lengths a factor of 2 smaller, central surface brightnesses which are 0.75 mag brighter, and total luminosities which are 0.75 mag. fainter compared to disks forming at $z \sim 0$. These predictions are similar to our HDF TF evolution, the TF evolution of Vogt et al. and the surface brightness evolution of Forbes et al. and Vogt et al, but not with the TF evolution found by Rix et al. and Simard & Pritchet. It is likely that some combination of size and luminosity evolution is taking place, probably in different proportions for galaxies of different luminosities and morphological types.

9. CONCLUSIONS

Galaxy-galaxy lensing is a powerful tool for probing the structure of dark matter halos at intermediate redshift. In this paper, we have detected the lensing signal due to the dark matter halos of galaxies at the 99.3% confidence level. An important feature of our analysis is the use of photometric redshifts to separate foreground and background galaxies, to determine the relative distances between them, and to obtain absolute magnitudes of the lens galaxies.

The scaling between lens galaxy halo circular velocity and galaxy B luminosity is consistent with a TF relation with the same slope $\eta = 0.35$ (or 7.14 in magnitudes per log circular velocity) as is observed locally. The typical lens galaxy, at a redshift $z = 0.6$, has a circular velocity of $210 \pm 40 \text{ km s}^{-1}$ at a rest-frame B magnitude $M = -18.5$.

A number of control tests, in which lens and source positions and source ellipticities are randomized, confirm the significance level of the detection quoted above. Furthermore, a marginal signal is also detected from an independent, fainter sample of source galaxies without photometric redshifts. If the two source samples are considered together, the lensing detection is significant at the 99.8% confidence level. Potential systematic biases, such as contamination by satellite galaxies, distortion of the source shapes by the light of the foreground galaxies, PSF anisotropies, and contributions from mass distributed on the scale of galaxy groups and on larger scales, were examined and are shown to be negligible.

Our HDF lens sample includes all morphological types but is dominated by spiral galaxies ~ 1 mag. below L_* . By comparing the lensing B -band TF relation to that of local

⁷ The difference between these results and the evolution -0.4 mag. quoted by Vogt et al. (1997) for their high-quality data arise from the different q_0 (they adopted 0.05) and an error in the inclination corrections (see Vogt et al. 1998) used by Vogt et al. (1996, 1997).

spirals, we find that at a fixed circular velocity, the intermediate redshift galaxies are somewhat fainter (by 1.0 ± 0.6 B mag) than they are nearby. This result is consistent with the study of rotation curves of intermediate-redshift spirals by Vogt et al. The lack of brightening of individual galaxies, coupled with the strong evolution in the global luminosity density suggests that the latter is dominated by evolution in the galaxy number density.

The sizes of the dark matter halos are less well constrained than the circular velocity due to the small size of the field. Indeed, almost any truncated isothermal model a mass of $2.8 \pm 1.2 \times 10^{11} h^{-1} M_{\odot}$ within $30 h^{-1}$ kpc is an acceptable solution. The prospects for galaxy–galaxy lensing based on wide-field multi-color imaging data are extremely promising: the wide ranges of separations should allow a determination of the halo dark matter density in the outer

regions at $\sim 100 h^{-1}$ kpc. On these scales the dark matter halos of individual galaxies may merge into a common group or cluster halo. The problem of determining where dark matter halos end may consequently prove to be more complicated, but no less important, than was originally anticipated.

We thank the referee for useful suggestions which improved this paper. MJH acknowledges financial support from a CITA National Fellowship and from NSERC of Canada through operating grants to F. D. A. Hartwick and C. J. Pritchett. SDJG gratefully acknowledges financial support from his supervisor F. D. A. Hartwick. HD acknowledges support from a PhD research grant provided by the Research Council of Norway.

REFERENCES

- Bertin, E., & Arnouts, S. 1996, *A&A*, 117, 393
 Bruzual A., G. & Charlot, S. 1993, *ApJ*, 405, 538
 Brainerd, T. G., Blandford, R. D., & Smail, I. 1996, *ApJ*, 466, 623 (BBS)
 Broeils, A. H. 1992, PhD thesis, Univ. Groningen
 Courteau, S. 1997, *AJ*, 114, 2402
 Dell’Antonio, I. P., & Tyson, J. A. 1996, *ApJ*, 473, L17 (DT)
 Ellis, R. S., Colless, M., Broadhurst, T., Heyl, J., & Glazebrook, K. 1996, *MNRAS*, 280, 235
 Faber, S. M., Wegner, G., Burstein, D., Davies, R. L., Dressler, A., Lynden-Bell, D., & Terlevich, R. J. 1989, *ApJS*, 69, 763
 Ferguson, H. C., & McGaugh, S. S. 1995, *ApJ*, 440, 470
 Forbes, D. A., Phillips, A. C., Koo, D. C., & Illingworth, G. C. 1996, *ApJ*, 462, 89
 Gwyn, S. D. J., & Hartwick, F. D. A. 1996, *ApJ*, 468, L77
 Hoekstra, H., Franx, M., Kuijken, K., Squires G. 1997, preprint (astro-ph/9711096)
 Hogg, D. W., et al. 1998, *AJ*, in press
 Jain, B., & Seljak, U. 1997, *ApJ*, 484, 560
 Kaiser, N., Squires, G., & Broadhurst, T. 1995, *ApJ*, 449, 460
 Lilly, S. J., Tresse, L., Hammer, F., Crampton, D. & Le Fevre, O. 1995, *ApJ*, 455, 108
 Lilly, S. J., Le Fevre, O., Hammer, F., & Crampton, D. 1996, *ApJ*, 460, L1
 Luppino, G. A. & Kaiser, N. 1997, *ApJ*, 475, 20
 Madau, P. 1995, *ApJ*, 441, 18
 Mao, S., Mo, H. J., & White, S. D. M. 1997, preprint (astro-ph/9712167)
 Marzke, R. O., Geller, M. J., Da Costa, L. N., & Huchra, J. P. 1995, *AJ*, 110, 477
 Mo, H. J., Mao, S., & White S. D. M. 1997, preprint (astro-ph/9707093)
 Rix, H.-W., Guhathakurta, P., Colless, M., & Ing, K. 1997, *MNRAS*, 285, 779
 Schade, D., Carlberg, R. G., Yee, H. K. C., Lopez-Cruz, O., & Ellingson, E. 1996a, *ApJ*, 464, L63
 Schade, D., Lilly, S. J., Le Fevre, O., Hammer, F., & Crampton, D. 1996b, *ApJ*, 464, 79
 Schade, D., Carlberg, R. G., Yee, H. K. C., Lopez-Cruz, O., & Ellingson, E. 1996c, *ApJ*, 465, L103
 Schneider, P., & Rix, H.-W. 1997, *ApJ*, 474, L25
 Simard, L., & Pritchett, C. J. 1998, *ApJ*, in press
 Tully, R. B., & Fouqué, P. 1985, *ApJS*, 58, 67
 Tyson, J. A., Valdes, F., Jarvis, J. F., & Mill, A. P., Jr. 1984, *ApJ*, 281, L59
 de Vaucouleurs, G., de Vaucouleurs, A., Corwin, H. G., Buta, R. J., Paturel, G., & Fouqué, P. 1991, *Third Reference Catalogue of Bright Galaxies* (Springer, New York)
 Vogt N. P., Forbes, D. A., Phillips, A. C., Gronwall, C., Faber, S. M., Illingworth, G. D., & Koo, D. C. 1996, *ApJ*, 465, L15
 Vogt N. P., et al. 1997, *ApJ*, 479, L121
 Vogt N. P., et al. 1998, in preparation
 Williams, R. E., et al. 1996, *AJ*, 112, 1335
 Willick, J. A., Courteau, S., Faber, S. M., Burstein, D., Dekel, A., & Strauss, M. A., 1997, *ApJS*, 109, 333
 van den Bergh, S., Abraham, R. G., Ellis, R. S., Tanvir, N. R., Santiago, B. X., & Glazebrook, K. G., 1996, *AJ*, 112, 359,
 Worthey, G. 1994, *ApJS*, 95, 107